ORIGINAL PAPER

Experiment and Numerical Modeling of Current Distributions Inside REBCO Tapes of No-Insulation Superconducting Magnet Coils Under Time-Varying Fields

Zhuoyan Zhong[1] · **Wei Wu**[1] · **Zhiyong Hong**[1] · **Zhijian Jin**[1]

Abstract

The current densities flowing in high-temperature superconducting wires are mostly non-uniform during operations (caused by the screening current effect). This is a major challenge to high-field superconducting magnets based on $(RE)Ba_2Cu_3O_{7-x}$ (REBCO; RE, rare earth) tapes, as to cause (a) uncertainty of the field distribution and (b) concentrated uneven Lorentz force that damages the magnet. For no-insulation (NI) REBCO coils, the current distribution would be even complicated when external time-varying fields induce extra transport current circulating in NI coils. For this study, a numerical model is established, and the results are compared with hall sensor measurements for an NI coil sample. Different with conventional insulated coils, for NI coils, it was measured that the variation of *axial* fields (parallel to REBCO surface) could introduce remnant current densities persisting on REBCO tapes, which generate remnant fields. These remnant fields would cause the distortion of the spatial field distribution of a magnet, and were also measured to exhibit constant field decay with logarithmic time. These remnant fields pose extra concerns for NI coils for applications in NMR/MRI magnets in terms of threatening the spatial field homogeneity and temporal field stability of these magnets. Practical cases are simulated, i.e., NI coils are under time-varying fields generated by its adjacent NI coils or background magnets during quench/fault. The induced current (and the resulted Lorentz forces) concentrates on one-side edge of REBCO tapes that is adjacent to the quenched/fault coils; this observation helps understand and protect the mechanical damage observed in recent operations of NI REBCO magnets.

Keywords HTS magnets · No-insulation coils · Current distribution · Screening current effect · NI coil quench

1 Introduction

The copper-oxide-based high-temperature superconductor (HTS) $(RE)Ba_2Cu_3O_{7-x}$ (REBCO; RE is rare earth) coils have been widely applied in high-field magnets. Besides, since the no-insulation (NI) winding technique was introduced [1], a number of high-field REBCO magnets have been designed and operated. Such magnets include the 1.3 GHz nuclear magnetic resonance (NMR) magnet [2], the 32.5 T all-superconducting magnet [3], and the world-record 45.5 T DC magnet [4]. The NI winding technique, due to the absence of the turn-to-turn insulation, makes the

REBCO coil become compact, mechanically robust, and self-protecting [5–7].

For REBCO magnets, the non-uniform current distribution (caused by the screening current effect) is widely regarded as a major challenge [2, 4, 8–11]. As seen in Fig. 1a, screening currents are induced by time-varying fields (external fields or coil self-fields) in the radial direction (B_r) [10, 11]. For superconductors, due to the extremely low resistivity, the screening current would persistently circulate on the conductor surface with little decay. Therefore, the current densities in superconductors are the superposition of transport currents (assumed to be uniformly distributed along coil axis) and screening currents, thus causing the current distribution usually non-uniform. The negative impacts of the non-uniform current distribution on the REBCO magnet involve two aspects. First, the combination of the high axial field and screening currents would cause excessive Lorentz forces (F_L, see Fig. 1a), which poses threats to the mechanical strength of the REBCO magnet [9,

✉ Wei Wu
Wei.Wu@sjtu.edu.cn

1   School of Electronic Information and Electrical Engineering, Shanghai Jiao Tong University, Shanghai 200240, China
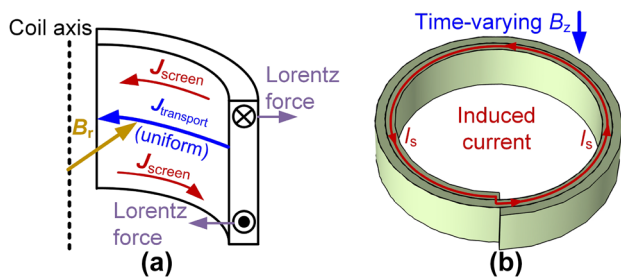
Fig. 1 a The overall current distribution of the superconductor is decomposed into transport currents (assumed to be uniformly distributed along coil axis) and screening currents. **b** For NI coils (not applicable for conventional insulated coils), the unexpected B_z during real operations would further change the current distribution by causing an induced current circulates in the coil through the non-insulated turn-to-turn contact

10, 12]. Second, the error field generated by the screening current (SCF) would cause the distortion of the spatial field distribution of a magnet [2, 13–17]. As shown in Eq. (1), the spatial field distribution ($\vec{B}$) of a REBCO magnet is composed by the error field from screening current ($\vec{B}_{\text{SCF}}$) and the field from the transport current ($\vec{B}_{\text{trans}}$) obtained by assuming the overall current distribution is uniform. The significant negative impact of screening current to the field quality of NMR magnets has been reported [2, 11, 16, 17].

$$\vec{B} = \vec{B}_{\text{SCF}} + \vec{B}_{\text{trans}} \tag{1}$$

The non-uniform current distribution of the conventional insulated (INS) REBCO coils has been well studied [10–16]. However, different from conventional INS coils, for NI HTS coils, the variation of axial field (B_z) would further reshape the current distribution. As shown in Fig. 1b, B_z would induce spiral current (I_s) circulating in NI HTS coils through the non-insulated turn-to-turn contact [18, 19]. Note that this induced I_s is a transport current, and should be distinguished from the screening current described in this work. This behavior complicates the local current distribution inside the HTS tape, which is still not clarified.

In real experimental operations, NI HTS coils, when used as insert magnets, could be under external time-varying fields from the quench/fault of background magnets (including low-T_c superconducting (LTS) and resistive magnets) [20–24]. Besides, inside a multi-pancake NI HTS coil, quench in one NI pancake leads to almost total loss of its spiral current responsible for magnetic field generation [5]. Thus, during quench propagation, an NI pancake suffers time-varying fields when its adjacent NI pancake quenches [4, 5, 25–28]. These recent studies give the concern that strong Lorentz forces can be caused by the large induced current in NI HTS coils resulted from the field variation. This factor was

considered to contribute to the irreversible mechanical damage of many high-field NI HTS magnets [4, 20–23, 27–29]. Previous works have made the calculations of the overall values of the induced I_s distributed among different pancakes/turns based on the 1D circuit-grid models [26–30]. However, there are prevalent requirements for the calculations with the consideration of the screening current effect [20, 23, 29, 30], which means to clarify the local non-uniform current distribution inside the conductor. This is important because the local concentration of the current densities (especially the concentration of the extra induced I_s) would result in the substantial enlargement of the Lorentz forces and stress/strain [10, 12]. However, this pursuit is limited by the previous simulation technique [29] and little essential progress has been made until now.

The purpose of this work is to clarify the non-uniform current distribution in NI HTS coils under time-varying fields. Two aspects are concerned: (a) the impact of the change of non-uniform current distribution on the main field generated by the REBCO magnet; (b) the effect of the distribution of the induced current (shown in Fig. 1b) on the potential Lorentz force damage of the REBCO magnet. In Sect. 3, the finite-element model proposed by Mataira et al. [31] was improved to allow the calculation of more refined current distributions of NI HTS coils (i.e., the current penetration depth could vary among different turns). In Sect. 4, the simulation and experiment results are presented to reveal the basic characteristics of current distribution, and its practical impact on REBCO magnet. In Sect. 5, simulations are conducted for several practical cases of NI REBCO coils under time-varying fields.

2 Experimental Setup

The HTS tape was 180-μm thick and 6-mm wide, and comprised two 50-μm copper layers, one 80-μm Hastelloy layer, and one 1-μm-thick and 4.75-mm-width REBCO layer, provided by Shanghai Superconductor. The sample was a 2×28 turn double-pancake (DP) NI coil. The length of the HTS tape was 10 m. In Fig. 2a, the measured V-I curve of the NI coil sample is shown by the black blocks, which is measured with the ramping rate of 0.2 A/s. Based on the criterion of 1 μV/cm, the critical current (I_c) of this HTS coil was 84 A at 77 K. The in-plot shows the picture of the NI coil sample. Figure 2b shows the central field of the NI coil during the sudden discharge test. Then, the contact resistivity (ρ_t) is calculated by Eq. (2) to be 32.4 $\mu\Omega\cdot\text{cm}^2$ [18]:

$$R_c = \sum_{i=1}^{N} \frac{\rho_t}{2\pi r_i w}, \quad \tau = \frac{L}{R_c} \tag{2}$$
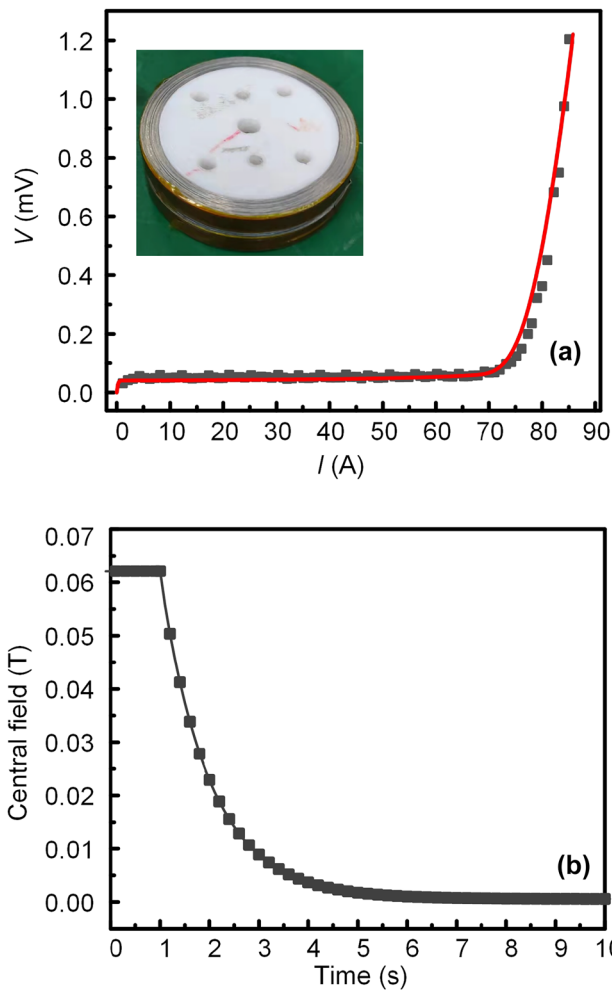
Fig. 2 **a** *V-I* curve of the NI coil sample measured with the ramping rate of 0.02 A/s. The black blocks are the measured points. The red lines are the simulated results. The in-plot shows the picture of the NI coil sample. **b** The field decay curve at the center of the NI coil during the sudden discharge test

Fig. 3 **a** Sketch of the experimental setup; the positions of hall sensors; the picture of the experimental setup. **b** Equivalent circuit diagram of the experimental setup, showing the coupling between the NI coil and copper coils

where N is the overall turn of the DP coil, w is the width of the HTS tape, r_i is the radius of each turn, τ is the time constant of the field decay to be 1005 ms, and L is the inductance of the NI coil to be 2.16×10^{-4} H.

The experimental setup is shown in Fig. 3a. Two copper coils represent the quenched NI HTS coils, or background magnets, applying time-varying fields to the NI coil sample. Hall sensors were arranged at positions P1–P4, in order to imply the current distribution. P4 was used to measure B_z, whereas P1–P3 were for measuring B_r. Fields at P1 and P2 are measured by the transverse-type hall sensor (HMCA-3160-WN) and at P3 and P4 are measured by the axial-type hall sensor (HMCA-2560-WN) manufactured by Lakeshore. The hall sensors are attached to the Gauss meter of Lakeshore Model 425. This arrangement was tested at 77 K with a liquid nitrogen cryostat. Figure 3b shows the equivalent
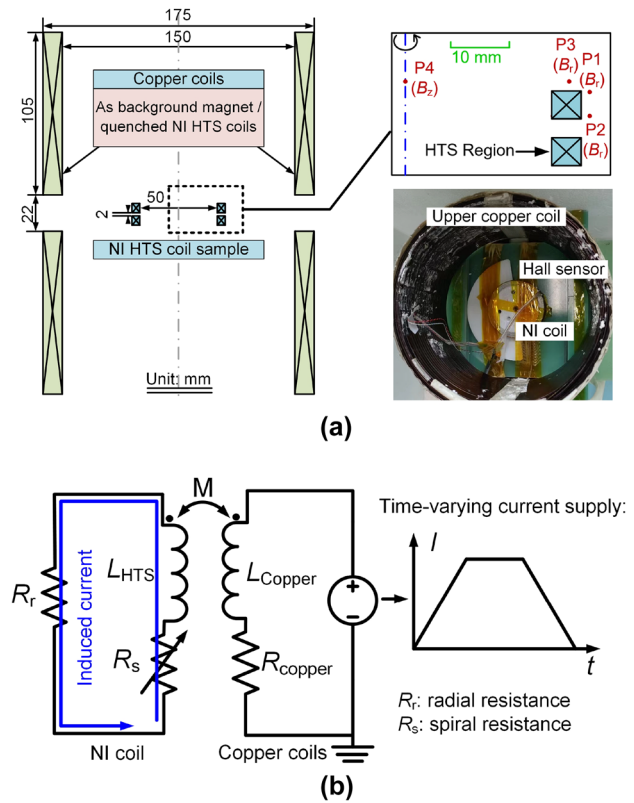
circuit of the NI coil coupled with the copper coils. It can be seen that the induced current in the NI coil is introduced by the mutual inductance in the NI coil with the copper coils.

The experimental procedure is described as follows. Time-varying fields are applied by copper coils. The HTS coil was not connected to any power source. The applied field is predominantly B_z to give clear observations of only the fields generated by the induced current. This is testified by a very slow ramp-and-down of applied field (0.05 mT/s, thus B_z being unable to cause induced current), and B_r was testified so weak to induce any measurable SCF at P1–P4. The hall sensors monitored the field variations during the entire process at a sampling rate of 100 Hz.

3 Numerical Model

The finite-element method (FEM) model is based on the H-formulation using the rotated anisotropic resistivity method recently proposed by Mataira et al. [31–33]. The governing equation is the H-formulation [34] shown in Eq. (3) that is derived from the Maxwell equations. The H, E, J, ρ_{coil}, and μ represent the magnetic field intensity,

electrical field, current density, resistivity, and the permeability of materials, respectively. To simulate the radial current (J_r) of NI coils, all three field components (H_r, H_z, and H_{phi}) are considered the independent variables in the *H*-formulation model.

$$\begin{cases} \nabla \times \mathbf{E} = -\mu \cdot \dfrac{\partial \mathbf{H}}{\partial t} \\ \nabla \times \mathbf{H} = \mathbf{J} \\ \mathbf{E} = \rho_{coil} \cdot \mathbf{J} \end{cases}. \tag{3}$$

Both the NI and INS coil have the geometry as Fig. 4a. The INS coil is usually simplified to be modeled as the concentric turns as Fig. 4b. Without the modeling of the power source and spiral geometry, the transport current of each turn of the INS coil is applied by artificially setting the boundary condition. This is feasible for the INS coil because the transport current of each turn is a known variable equal to the operating current supplied by the power source. However, this simplification is commonly not applied for the NI coil, since the transport current of each turn is the unknown variable that can be different from the current supplied by power source (I_{PS}). If the NI coil is modeled as Fig. 4b, the equivalent circuit model must be coupled to calculate the transport current of each turn [35]. In this pure FEM model without the coupling with circuit model, the real coil geometry and the power source shown in Fig. 4a must be modeled. The modeling of the spiral coil in the 2D axisymmetric model is achieved by setting the resistivity matrix (ρ_{coil}) described as the following.

As seen from Fig. 4c, for the 2D axisymmetric model, the vectors in the governing equation (Eq. (3)) are in cylindrical coordinates in (r, ϕ, z). However, the direction of current flow of the coil is in (n, T, z), where n and T are the vectors that are normal and tangential to the surface of the superconductor tape, respectively. In Fig. 4c, α is the angle between the spiral winding direction (T) and circumferential direction (ϕ) of the cylindrical coordinate system, and is calculated by

$$\alpha = \pm \tan^{-1}\left(\frac{d}{2\pi r}\right), \tag{4}$$

where d is the thickness of the HTS tape, and r is the local radius inside the HTS coil. Then, according to Fig. 4c, the (E_r, E_ϕ, E_z) is expressed by (E_n, E_T, E_z) as:

$$\begin{bmatrix} E_r \\ E_\phi \\ E_z \end{bmatrix} = \begin{bmatrix} \cos\alpha & \sin\alpha & 0 \\ -\sin\alpha & \cos\alpha & 0 \\ 0 & 0 & 1 \end{bmatrix} \begin{bmatrix} \rho_n J_n \\ \rho_{sc} J_T \\ \rho_{sc} J_z \end{bmatrix}, \tag{5}$$

where ρ_n is the turn-to-turn contact resistivity in $\Omega \cdot m$. Generally, the contact resistivity extracted from the measurement is the surface resistivity in $\mu\Omega \cdot cm^2$ (signified as ρ_t). In this model, ρ_n in $\Omega \cdot m$ is the bulk resistivity homogenized across the thickness between two superconducting layers. The derivation of ρ_n from ρ_t is given by $\rho_n = \rho_t/t$, where t is the thickness of the HTS tape.

The ρ_{sc} is the superconductor resistivity. The ρ_{sc} is described by the *E-J* power law [36] with $E_c = 1$ $\mu V/cm$ and a measured *n* value of 21, shown in:

$$\rho_{sc} = \frac{E_c}{J_c(B_{per}, B_{par})} \left| \frac{J_{sc}}{J_c(B_{per}, B_{par})} \right|^{n-1}, \tag{6}$$

where J_{sc} is the current density flowing in the plane of the superconductor given by $(J_T^2 + J_z^2)^{1/2}$. The dependence of critical current density on magnetic field, $J_c(B_{per}, B_{par})$, of HTS tapes is depicted by the Kim equation [37] shown in Eq. (7). The B_{per} and B_{par} indicate the field perpendicular and parallel to the surface of HTS tapes, respectively. The I_c of the single HTS tape in its self-field is measured to be 160 A. Therefore, the parameter J_{c0} is 3.37×10^{10} A/m^2, which is obtained by the I_c divided by the cross-section of the HTS tape. The other parameters *k* and *b* are set to be 0.29 and 0.8, respectively, which are typical values for the GdBCO tapes manufactured by Shanghai Superconductor at 77 K [38, 39]. The B_c was testified to be 0.061 T, since the simulated *V-I* curve based on this parameter (see red line in Fig. 2a) can be consistent with the measurement result (see black blocks in Fig. 2a).

$$J_c(B_{per}, B_{par}) = J_{c0} / \left(1 + \frac{\sqrt{k^2 B_{par}^2 + B_{per}^2}}{B_c}\right)^b. \tag{7}$$

Then, for Eq. (5), $[J_T \ J_n \ J_z]^T$ is expressed by:

$$\begin{bmatrix} J_n \\ J_T \\ J_z \end{bmatrix} = \begin{bmatrix} \cos\alpha & -\sin\alpha & 0 \\ \sin\alpha & \cos\alpha & 0 \\ 0 & 0 & 1 \end{bmatrix} \begin{bmatrix} J_r \\ J_\phi \\ J_z \end{bmatrix}. \tag{8}$$
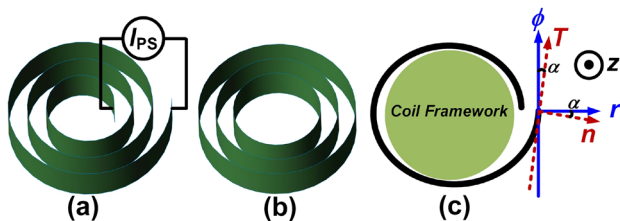

Fig. 4 **a** Real geometry of the HTS coil. **b** The traditional approximation of the HTS coil by the concentric turns. **c** Comparison of the spiral winding direction (n, T, z) to the cylindrical coordinate system (r, ϕ, z). n and T are the vectors that are normal and tangential to the surface of the superconductor tape, respectively

Eventually, the resistivity matrix (ρ_{coil}) that enabled the modeling of the real spiral geometry of HTS coils in the cylindrical coordination, is derived as:

$$\rho_{coil} = \begin{bmatrix} \rho_{rr} & \rho_{r\phi} & 0 \\ \rho_{\phi r} & \rho_{\phi\phi} & 0 \\ 0 & 0 & \rho_{sc} \end{bmatrix} r, \phi, z, \quad (9)$$

where the parameters ρ_{rr}, $\rho_{r\phi}$, and $\rho_{\phi r}$ are:

$$\begin{cases} \rho_{rr} = \rho_n \cos^2(\alpha) + \rho_{sc} \sin^2(\alpha) \\ \rho_{\phi\phi} = \rho_{sc} \cos^2(\alpha) + \rho_n \sin^2(\alpha) \\ \rho_{r\phi} = \rho_{\phi r} = \frac{1}{2}(\rho_{sc} - \rho_n) \sin(2\alpha). \end{cases} \quad (10)$$

In this simulation, both the HTS and copper coils are modeled. The detailed geometry is identical with Fig. 3a. The *H*-formulation model adopts the second-order element, in order to obtain the more refined current distribution.

4 Results and Analysis

4.1 Current Distribution

Figure 5a shows the field applied by copper coils at the center of the HTS coil (i.e., B_z at P4) measured in room temperature; the direction of the applied field was downward in Fig. 5c as indicated by the hollow white arrows. The applied field was ramped up in 0.25 s and held for a while, and then decreased to zero in 0.25 s. Figure 5b shows the calculated average spiral current (I_s) in the NI HTS coil. During the increase and decrease of external B_z (shown in Fig. 5a), spiral current I_s can be induced in the NI HTS coil. As the B_z stabilizes, the I_s decays to zero through the turn-to-turn resistance. We also show the results calculated from the well-verified circuit-grid model [19] with four elements per turn, which examined the correctness of this finite-element model.

Figure 5c shows the calculated current (colors) and field (arrows) distributions in the cross-section of the HTS coil at the key moments (t_1, t_2, t_3, t_4). For each cross-section, the axis of the HTS coil is on the left. For better visibility of B_r, the field distribution (the arrows) only shows the self-field of the HTS coil that excludes the large B_z from copper magnets. At $t = t_1$, positive red currents are induced as the I_s increases (see Fig. 5b). At $t = t_2$, with the decay of the I_s, the current density is essentially not decreased, but negative blue current densities are created. This resembles current distributions in HTS coils connected to current supply when the power source current is decreasing [12, 31]. The current distributions at (t_3, t_4) are similar to those at (t_1, t_2) but with current
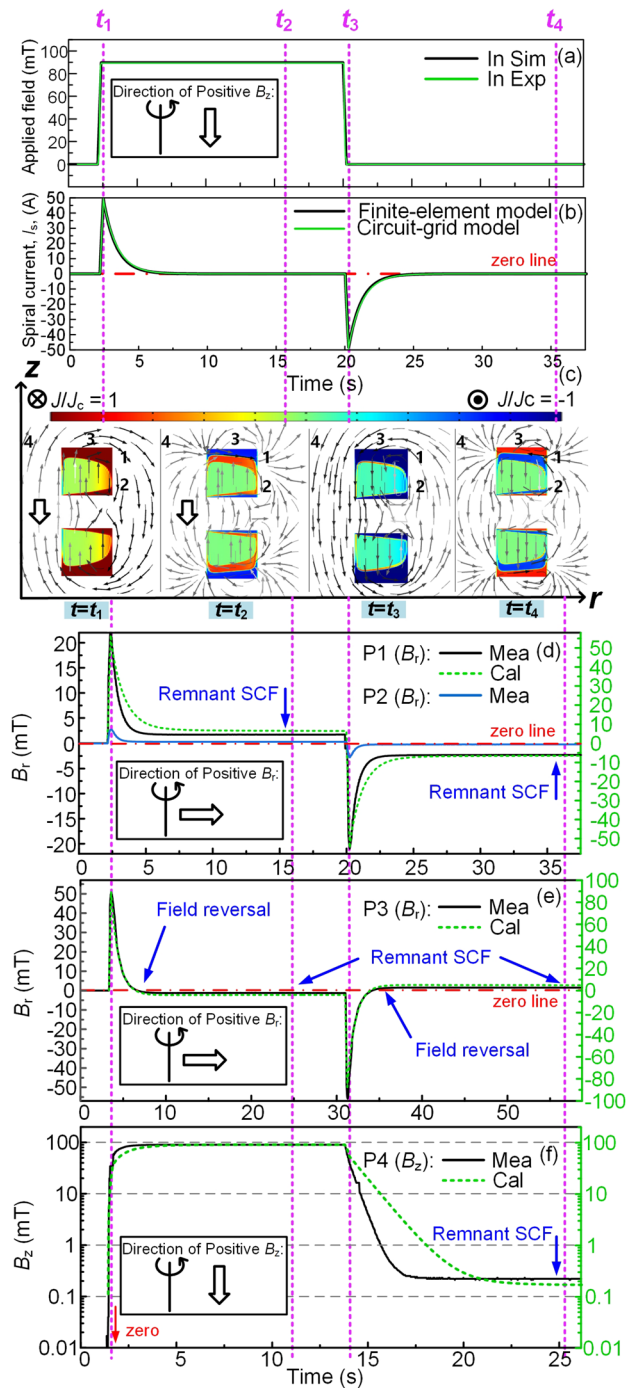

Fig. 5 Measured and calculated results. **a** The applied field by copper coils at the center of HTS coil (i.e., B_z at P4). **b** Calculated average I_s of the NI HTS coil. **c** Current (colors) and field (arrows) distributions in the cross-section of the HTS coil at the key moments (t_1, t_2, t_3, t_4). For each cross-section, the axis of the HTS coil is on the left. The hollow arrows indicate the direction of applied external B_z. For better visibility of B_r, the field distribution only shows the self-field of the HTS coil and excludes the large B_z from copper magnets. **d**–**f** The measured and calculated magnetic fields at P1–P4; the positions of P1–P4 are also roughly shown in Fig. 5c. Note that the time scales of (d–f) are different; thus, the t_1–t_4 are only general qualitative notations of time

densities in reversed direction. At t_2 and t_4, although the integrated transport current of the coil is zero, it is noteworthy that remnant current densities persist in the HTS coil. These generate a remnant magnetic field (see arrows).

The mechanism of the generation of the remnant current densities at t_2 and t_4 was studied. The current densities at t_2 and t_4 are all screening currents, because the integrated transport current of the coil (I_s) is zero in these moments according to Fig. 5b. These remnant current densities (i.e., screening currents) were induced by the B_r component of the coil self-field previously established by the induced I_s (during the time that the induced I_s has not decayed to zero). So, the generated SCF (see arrows in Fig. 5c at t_2 and t_4) tends to keep the coil self-field previously established by the induced I_s (see arrows in Fig. 5c at t_1 and t_3), respectively.

For conventional insulated HTS coils, only B_r (perpendicular to HTS tapes) could induce a screening current, as seen in Fig. 1a. However, for NI HTS coils, it was found that the variation of B_z (parallel to HTS tapes) would also induce a new screening current like shown in Fig. 5c at t_2 and t_4 by an indirect way mentioned in the above paragraph. In other words, the remnant current densities shown in Fig. 5c at t_2 and t_4 would only exist in NI coils, while for conventional INS coils, the current density would be almost constantly zero (testified with simulation). These remnant current densities would generate additional error fields during later operations, as shown by arrows of Fig. 5c at t_2 and t_4. The spatial distribution of these remnant fields can introduce harmonic errors to the spatial field distribution of the NMR and magnetic resonance imaging (MRI) magnets [2, 10, 16, 17], for which the excellent spatial field homogeneity is required. The measurement and analysis of the impact of these remnant error fields on magnet applications are shown in the following Sects. 4.3 and 4.4.

4.2 Magnetic Field Measurement

Figure 5d–f shows the measured magnetic fields at P1–P4 (see solid black/blue lines) and the simulation results (see green dashed lines). The measurement is to validate the basic characteristics of the simulated current distributions. So, only qualitative comparison is required. The quantitative agreement between simulation and experiment is not pursued in this work, which could be affected by many factors, such as (i) the field-dependent of the I_c of the HTS tape has not been precisely measured and then adopted in the simulation; (ii) the contact resistivity can be usually non-uniform [40]; and (iii) the location of the hall sensor at P1–P4 in the measurement might have slight deviation. In addition, it can be seen that the simulation shows discrepancy with the measurement for the slopes of the field curves. The slopes of the field curves, such as the field decay curves in Fig. 5d and f during (t_1, t_2) and (t_3, t_4), are dependent on the characteristic time

constant of the NI coil [18], which is decided by the turn-to-turn contact resistivity. In the simulation, the ρ_t is always set to be 32.4 $\mu\Omega\cdot cm^2$. The measurement was conducted in the order of Fig. 5e → d → f, and after each measurement, the HTS coil is warmed to room temperature to erase the remained historical current densities, and then cooling down to 77 K to begin the next measurement. It has been widely reported that this thermal cycling enhances the turn-to-turn resistivity (ρ_t) [25, 41]. So, the ρ_t value of the NI coil might have changed during the measurement of Fig. 5d–f, thus deviating from the initially measured ρ_t value of 32.4 $\mu\Omega\cdot cm^2$.

Still, the basic characteristics of current distribution could be verified by the qualitative agreement between simulation and experiment, as analyzed below. In Fig. 5d, B_r measured at P1 is much stronger than at P2, indicating that most induced I_s concentrates on the edge of P1, whereas few current densities are on the edge of P2. Between (t_1, t_2), at P1, it can be seen that B_r decreases with the decay of induced I_s (see Fig. 5b), but B_r never approaches to zero. Remnant B_r can be measured at t_2. This verifies the existence of remnant current densities shown in Fig. 5c at $t = t_2$. In Fig. 5e, between (t_1, t_2), the B_r at P3 decreases and then reverses to the negative direction. This indicates that a negative current density was created as shown in Fig. 5c at $t = t_2$. For Fig. 5d and e, the analysis of the B_r waveforms between (t_3, t_4) is similar with (t_1, t_2), thus not being presented.

Figure 5f shows the B_z at P4 (note that P4 is at the coil center which is much further away from the HTS region than that shown in Fig. 5c). The increase and decrease in the B_z exhibit a lag compared to the applied field (see Fig. 5a). This is because the induced I_s in the NI HTS coil resists changes in the applied field. Especially, at $t = t_4$, although the overall transport current of the coil is zero, the remnant B_z about 0.22 mT could be measured, which is generated by the remnant current densities.

4.3 Remnant Magnetic Field

The remnant magnetic fields (marked as "remnant SCF" in Fig. 5d–f) are focused, since they would persistently change the main field generated by the magnet during the later operation. These remnant fields are all generated by screening currents, because the coil transport current is zero in these moments according to Fig. 5b at t_2 and t_4, and the coil current distribution is all screening currents. Especially, the remnant B_z at the coil center (at P4) would always be in the direction that resists the external B_z variation, like the remnant SCF marked in Fig. 5f and the arrows in Fig. 5c at t_2 and t_4. Thus, the central axial field generated by an NI REBCO magnet could be either enhanced or lowered depending on the direction of external B_z variation.

For NMR magnets, the NI REBCO coil design was favored as the insert magnet, and was operated in driven

mode [2, 17, 27, 42], rather than the persistent current mode [38, 39, 43]. For which, the field distribution was finely designed and regulated with field shims, in order to achieve the excellent spatial field homogeneity [2, 17]. However, the remnant error field (marked as "remnant SCF" in Fig. 5d–f and arrows in Fig. 5c at t_2 and t_4), which comes from the B_z variation, would make the field distribution of a magnet deviate from its design value, thus deteriorating the spatial field homogeneity of NMR magnets. The field quality is also crucial for the MRI and accelerator magnets in terms of the field precision, spatial homogeneity, and temporal stability [11, 44, 45]. Although the NMR/MRI magnets are working in stable magnetic field, one NI coil could feel B_z variation during the excitation/adjustment of the background magnet [22], non-synchronous excitation of HTS coils [42], or the typical quench-recovery process of an NI coil stacked in the insert magnet as shown later in Sect. 5.1.

4.4 Temporal Field Stability

The screening current would slowly decay due to the resistance of the superconductor (see Fig. 1a), leading to the variation of the magnetic field with time. However, for field quality-sensitive devices such as the NMR magnets, temporal field stabilities of the order of 10 ppb/h could be required [16]. For conventional INS coils, the field time variation due to the decay of screening currents induced by its self-radial-field has been measured [11, 13, 16]. The temporal field variation could not satisfy the stability requirement of NMR magnets until hundreds of days' relaxation [16], thus deteriorating the field quality of NMR magnets. In this work, it has been revealed in Sects. 4.2 and 4.3 that the B_z variation would cause remnant screening current densities on REBCO surfaces, which generate an additional field. The temporal stability of this field is measured.

Figure 6a shows the $|B_r|$ measured at P1 as a continuation of Fig. 5d. The time is set to zero upon the end time of Fig. 5d. Considering that the integrated transport current of the coil is zero at this instant, the measured field is contributed by only the screening current, and is regarded as the SCF. Figure 6a exhibits rapid field decay during the initial stage (i.e., the initial 10 s), and after which the field decay is much slower. After the exhaustion of liquid nitrogen, the SCF decays to zero quickly, since the resistance of the superconductor abruptly increases and the screening current decreases quickly.

Figure 6b shows the plot of Fig. 6a during $(10^1\ \text{s}, 10^4\ \text{s})$ in double logarithmic coordinates. It was found that the slope of field decay is constant in the double logarithmic plot. For the initial 10 s (not presented in Fig. 6b), the slope is not consistent with the following time shown in Fig. 6b. The reason might be the measurement error for the field decay rate during $(10^0\ \text{s}, 10^1\ \text{s})$ is much larger than during $(10^3\ \text{s},$
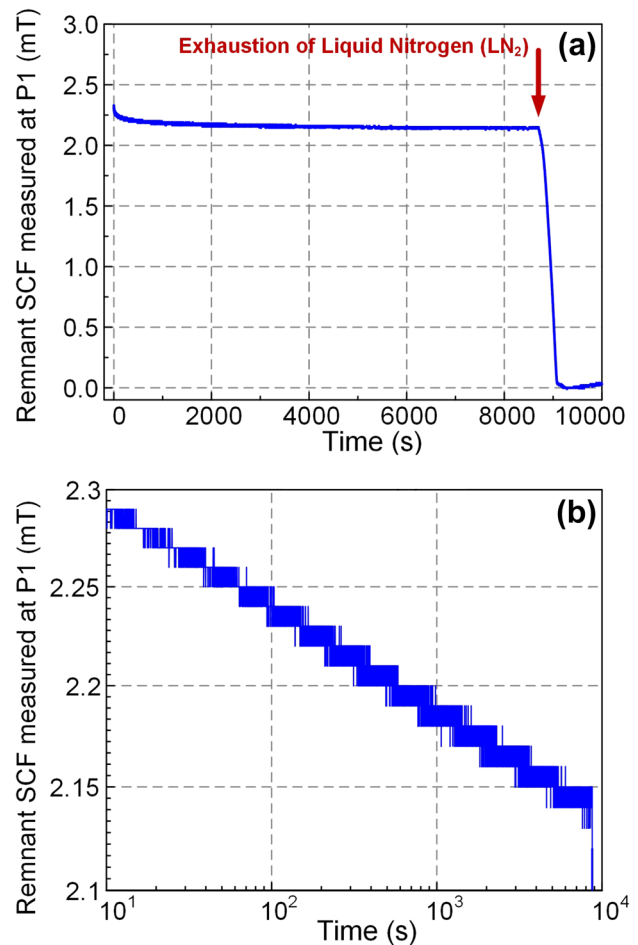

Fig. 6 Measured long-term transient variation of $|B_r|$ at P1 as a continuation of Fig. 5d after t_4: **a** in linear coordinates, **b** in double logarithmic coordinates within $(10^1\ \text{s}, 10.^4\ \text{s})$

10^4 s). The constant slope of the field decay plot could be well explained by the decay of the screening current due to the flux creep resistance of the superconductor, which has been reported to follow the constant decay rate in log–log plot as [15, 46]:

$$S = \frac{\partial \ln J(t)}{\partial \ln t} = \frac{1}{J(t)} \frac{\partial J(t)}{\partial \ln t} = -\frac{k_B T}{U_0} \tag{11}$$

where J is the current density of screening current, and k_B, T, and U_0 were the Boltzmann's constant, absolute temperature, and the pinning potential of the superconductor, respectively. The decay of the field is expected to follow the same logarithmic time dependence as the current density [15]. Besides, the field (current) decay per decade (i.e., $\partial J(t)/\partial \ln t$) could also be assumed to be constant according to Eq. (11), since the $J(t)$ does not vary a lot during $(10^1\ \text{s},$ $10^4\ \text{s})$. By this way, the field decay rate was evaluated to be almost constantly 0.05 mT per decade of time. The field decay amplitude would be even greater for the real-scale

ultra-high-field magnets. For the NI REBCO coils that are usually adopted as the insert magnets of NMR [2, 17, 27, 42], the axial field variations should be avoided considering that the temporal field variation would be caused by the new induced screening current.

5 Discussion

The studies presented in the above sections, i.e., the NI magnet under time-varying fields, can occur in practical applications. For example, the NI coil is under time-varying fields when its adjacent NI coil quenches, or the background magnet goes through a quench or fault. In this section, simulation results are presented to illustrate these practical conditions. Compared with the previous calculations for the NI coil quench [5–7, 26–30], this work clarifies the detailed local non-uniform current distribution inside the superconductor.

In these simulations, the HTS coil is assumed to be operated in 4.2 K. The critical current parameters in Eq. (7), k, B_c, J_{c0}, and b, were set to be 9.1×10^{-3}, 0.59 T, 2.65×10^{11} A/m^2, and 0.6, respectively. The ρ_t is set to be 54 $\mu\Omega\cdot$cm^2. For the quench simulation, this work is focused on the NI pancake in the magnet that is affected by time-varying fields. Conversely, the NI pancake in the magnet that generates the time-varying fields, i.e., the quenched NI pancake, is not focused. During the occurrence of quench, the heat disturbance affects the NI pancake by reducing the critical current of the superconductor. In this work, the thermal simulation is not conducted. Instead, as shown in Fig. 7, the J_{c0} of the whole quenched NI pancake is artificially set to decrease during the quench (i.e., t_1-t_2). It is assumed that the quench of the whole NI coil is achieved in 0.02 s, which is a common velocity of the quench propagation inside a single NI pancake [5]. Then, the pancake is recovered from the quench during (t_2, t_3), in which time the J_{c0} is artificially set to come back to its initial value. Section 5.1 studies the whole process of the quench-recovery (i.e., t_1-t_3), while Sect. 5.2 studies only the quench process (i.e., t_1-t_2).
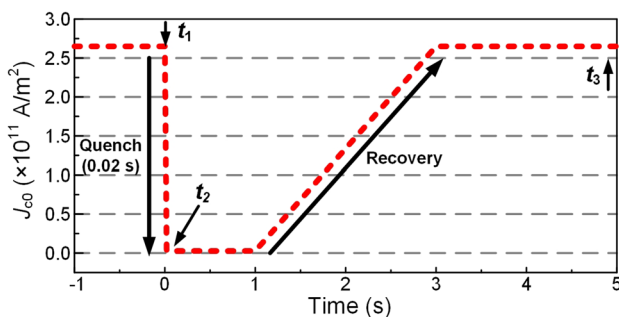
Fig. 7 Setting of the critical current parameter, J_{c0}, of the quenched NI pancake

5.1 Current Distribution Inside a Double-Pancake NI HTS Coil During Quench

The self-protecting characteristic makes NI coils highly attractive for magnet applications, in the sense that NI coils fully recovery after a quench without any external protection mechanism [5–7]. In this simulation, we present the current distribution inside a DP HTS coil during a typical quench-recovery process. For this case, the upper pancake is under time-varying fields from the quench-recovery of the lower pancake. The geometry of the DP HTS coil is identical with Fig. 3a. The HTS coil is connected to a power source that supplies the operating current $I_{PS} = 300$ A during the entire process. The lower pancake suffers a quench-recovery process due to the heat disturbance. Again, this process is simulated by setting the critical current as in Fig. 7.

The results of current distributions are shown in Fig. 8a. The simulated I_s of the lower pancake is shown in Fig. 8b, which indicates the waveform of the time-varying field experienced by the upper pancake. The I_s result in Fig. 8b is similar with the results in previous simulation based on the circuit model [5, 6].

In Fig. 8a, at $t = t_2$, as the lower pancake quenches, the average I_s of the upper pancake increases from 300 to 451 A. The increase of I_s is contributed by the induced current that circulates in the HTS coil through the non-insulated
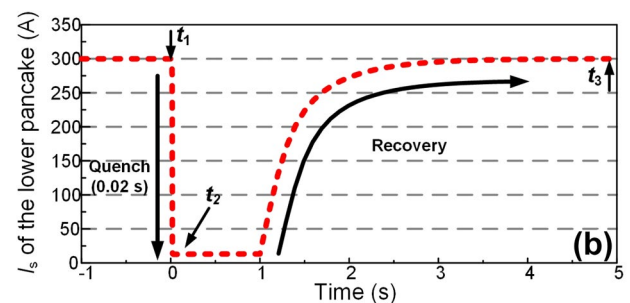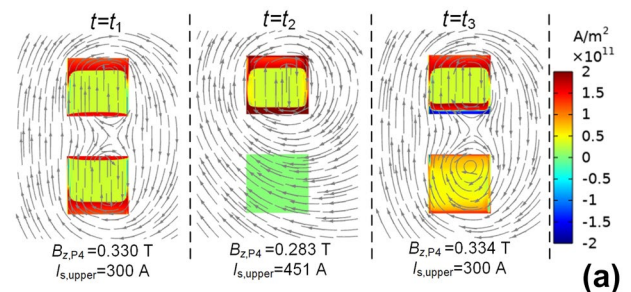
Fig. 8 **a** Distributions of current density of the HTS coil during quench-recovery at t_1, t_2, t_3, respectively. For each sub-figure, the axis of HTS coil is on the left. The parameter $B_{z,P4}$ indicates the on-axis field (i.e., B_z at P4), and $I_{s, upper}$ indicates the average spiral current of the upper pancake. **b** Simulated average spiral current (I_s) of the lower pancake during quench-recovery

turn-to-turn contact. It is observed that the induced I_s mainly concentrates on the lower tape edge of the upper pancake, which is the edge that faces the source of field variation (i.e., the quenched lower pancake). This phenomenon of current distribution is shaped by screening currents caused by B_r, but is also a reflection of Lenz's law.

At $t = t_3$, the I_s of both upper and lower pancakes has recovered to 300 A ($= I_{PS}$). For the upper pancake, again, even after the complete recovery, remnant current densities could be observed on the lower tape edge. For the lower pancake, notably, the current density is almost uniform, which deviates from the critical-state Bean model for non-ideal type-II superconductors [47]. The possible reason is that during the initial stage of recovery process, the spiral transport current of the lower pancake is always close to its critical current, leading to full penetration of current densities in HTS tapes.

In this case, the on-axis field (i.e., B_z at P4) is increased from 0.330 (before the quench-recovery at $t = t_1$) to 0.334 T (after the quench-recovery at $t = t_3$). Two factors attribute to the enhancement of the on-axis field: (1) the remnant current densities on the lower edge of the upper pancake, which helps generate upward magnetic fields; (2) elimination of screening currents on the lower pancake that cause the main field reduction [10, 11]. So, the typical quench-recovery process would cause the substantial change of the field distribution, which would threaten the high precision and spatial homogeneity of the field distribution of a finely designed NMR/MRI magnet, and should be avoided.

5.2 Current Distribution Inside a Multi-Pancake NI HTS Coil During Quench

As reported [4, 27, 28, 42, 48, 49], induced currents in NI HTS coils during inductive quench propagation cause strong Lorentz forces. To help understand and avoid this issue, we present the current distribution with the consideration of screening current effect, then the local concentration of the induced current (and the resulted Lorentz forces) could be clarified. Several HTS pancakes mentioned in Sect. 5.1 are stacked in series connections with the current supply $I_{PS} = 300$ A, as shown in Fig. 9a. Then, the quench is initiated in one pancake in this HTS magnet. Again, the setting of the critical current of the quenched pancake is as Fig. 7.

Figure 9b–e shows current distributions that different pancakes (Pan8–Pan5) of the HTS magnet are fully quenched at the moment $t = t_2$ (t_2 is marked in Fig. 7), respectively. The basic rule of current distribution can be conducted: the induced current of one HTS pancake mainly concentrates on the one-side edge that faces the quenched HTS pancake. This characteristic results in two types of current distributions. First, in Fig. 9e, for Pan4 and Pan6, induced currents and original power source currents (I_{PS}) concentrate
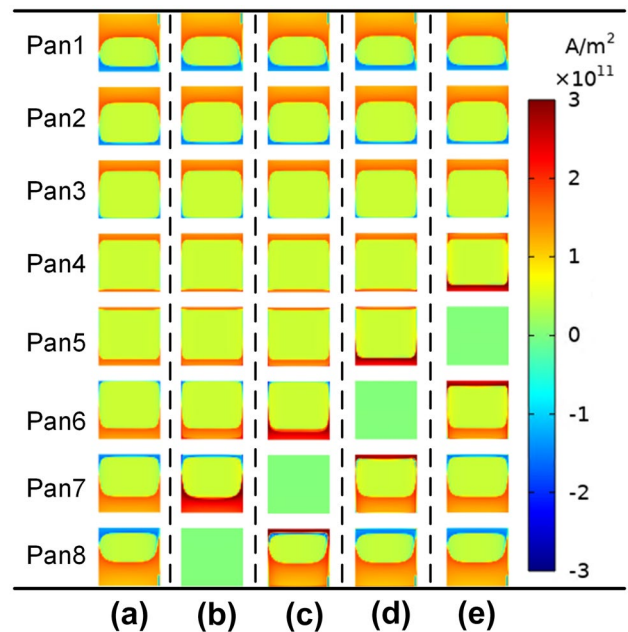

Fig. 9 a Current distribution at the moment $t = t_1$ that the multi-stacked coil has been charged to 300 A with 0.1 A/s. **b–e** Current distributions at the moment $t = t_2$ that different pancakes (Pan8–Pan5) of the HTS magnet are fully quenched, respectively. Note that the moments (t_1, t_2) are marked in Fig. 7

on different edges of the HTS tape. Second, in Fig. 9b, for Pan7, induced currents and the original I_{PS} concentrate on the same tape edge. The current distribution of the second case could cause substantially larger strain.

5.3 Current Distribution Inside a Multi-Pancake NI HTS Coil Under Background Magnet Fault

In recent experimental operations, NI HTS insert magnets are reported to be under time-varying fields from the quench of the LTS magnets [21–24], and the fault of resistive magnets [20]. In above cases, the variations of external fields are fast enough to cause large induced currents in NI HTS coils, and mechanical damages are widely reported. This section shows the simulated current distributions of two types of magnets during the background magnet fault: (i) the magnet with NI coil as the insert magnet; (ii) the magnet with INS coil as the insert magnet. The geometry and modeling parameters of the HTS coil are identical with which in Fig. 9. The real geometry of the background magnet is not modeled, and the field generated by the background magnet is simulated by artificially setting the Dirichlet boundary condition.

Figure 10a shows the magnetic field components at the center of the magnet contributed by the background magnet and HTS magnet during the background magnet fault, respectively. B_{BG} is the magnetic field contributed by the
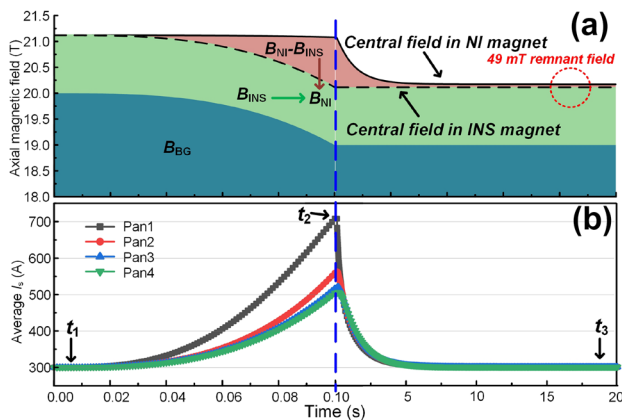
Fig. 10 **a** B_{BG}, field contributed by the background magnet; B_{INS}, field contributed by the INS HTS magnet; B_{NI}, field contributed by the NI HTS magnet. **b** For the NI HTS magnet: average spiral current (I_s) of Pan1–Pan4

background magnet. The B_{BG} is artificially set to decrease to simulate the fault of the background magnet. During this process, B_{INS} and B_{NI} are the field contributed by the HTS magnet based on the INS coil and NI coil, respectively. The dashed line and solid line indicate the central field of the magnets with the INS coil and NI coil as the insert magnet, respectively.

In the left half of Fig. 10a, the central field of the INS magnet (see dashed line) decreases synchronously with the reduction of background field, because the field generated by the INS magnet (B_{INS}) is always constant. However, the central field of NI magnet (see solid line) hardly decreases, because the induced current generates a field (i.e., B_{NI}-B_{INS}, see the red color) that resists background field reduction.

Figure 10b shows the average I_s of Pan1–Pan4 of the NI coil. The data of Pan5–Pan8 is not shown since it is identical with Pan4–Pan1, respectively. It is found that the bottom and top pancakes (Pan1 and Pan8) have much larger induced current. Thus, the top and bottom pancakes have higher risk to be injured by Lorentz forces generated by induced currents. At $t = t_3$, even though the induced current in the NI coil has decayed to zero, indicating that the transport current of the NI coil is identical with the INS coil, the field generated by the NI magnet is still 49 mT larger than the INS magnet (see Fig. 10a). This is caused by the difference in the current distributions of the NI coil and INS coil, which is subsequently analyzed by Fig. 11.

Figure 11 shows current distributions of HTS magnets at the key moments (t_1, t_2, t_3) marked in Fig. 10b. Figure 11a–c shows the current distribution for the NI magnet; for each pancake, the induced current is more likely to concentrate on the edge that faces outwards towards the ends of the HTS magnet. This phenomenon once attaches importance on the protection of these edges, like arranging HTS tapes
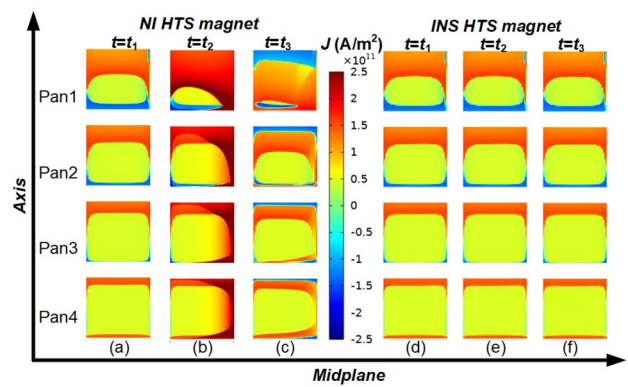

Fig. 11 Current distributions at the key moments (t_1, t_2, t_3) marked in Fig. 10b. Note that only the upper half of the HTS magnet is shown. **a**–**c** For NI magnets. **d**–**f** For INS magnets

with un-silt edges to face the ends of HTS magnets [4], and epoxy impregnation [9] for these edges. In Fig. 11d–f, the current distribution of the INS magnet has no essential variation during the whole process. Comparing Fig. 11c and f, although the transport current of the NI and INS coil is identical, the current distributions are essentially different. Again, similar with Fig. 5, this is because that the variation of the axial field causes extra remnant current densities in the HTS tape of the NI coil.

6 Conclusion

In summary, the current distribution of NI REBCO coils under time-varying fields was demonstrated in both simulations and experiments. The FEM model for the current distribution simulation of NI coils was improved for more refined current distribution, i.e., the current penetration depth could vary among different turns. Different from conventional INS coils, for NI coils, it was found that the external B_z variation would induce remnant current densities persisting on the REBCO surfaces, which generate a remnant field. The remnant error field would cause the distortion of the field distribution generated by a magnet, thus posing threat to the spatial field homogeneity of the finely designed NMR/MRI magnets. Besides, it was measured that this remnant magnetic field, as the SCF, decays with time due to the decay of screening current caused by the resistance of the superconductor. The decay amplitude is constant with logarithmic time. It would pose threats to NMR/MRI magnets, which require the temporal field stability to be in order of 10 ppb/h. Based on the above, the remnant field induced by external B_z variation should be an additional concern for NI coils for applications in the magnets that require high field quality.

Several practical cases of NI HTS coils under time-varying fields are investigated. First, we studied the current distribution

of a DP HTS coil when a typical quench-recovery process occurs on one NI pancake. For this case, the un-quenched pancake is under time-varying fields generated by the quenched pancake. It was found that the typical quench-recovery process for NI coils would substantially change the current distribution, causing the central field generated by a DP coil increased for several milli-tesla compared to which before this process. The change of current distribution after the quench-recovery includes that the current distribution of the quenched pancake becomes almost uniform, which deviates from the critical-state Bean model; besides, remnant persistent current densities are induced on the un-quenched pancake. Second, the current distribution is studied for a multi-pancake NI HTS coil when quench is initiated on one pancake. The time-varying field due to the pancake quench would cause induced currents in its nearby pancake(s). On these pancakes with induced currents, the induced current (and the resulted Lorentz forces) mainly concentrates on the one-side edge of the REBCO tapes that face the quenched pancake. This phenomenon helps understand and protect the mechanical damage usually observed in NI HTS magnets after inductive quench propagation. Third, a multi-pancake NI HTS coil under time-varying fields generated by the background magnet during fault was simulated. The induced current in each pancake mainly concentrates on the edges that face outwards towards the end of the magnet, which bring higher risk for these positions to be damaged by Lorentz forces.

References

1. Hahn, S., Park, D.K., Bascunan, J., Iwasa, Y.: IEEE Trans. Appl. Supercond. **21**, 1592 (2011)
2. Li, Y., Park, D., Yan, Y., Choi, Y., Lee, J., Michael, P.C., Chen, S., Qu, T., Bascuñán, J., Iwasa, Y.: Supercond. Sci. Technol. **32**, 105007 (2019)
3. Liu, J., Wang, Q., Qin, L., Zhou, B., Wang, K., Wang, Y., Wang, L., Zhang, Z., Dai, Y., Liu, H., Hu, X., Wang, H., Cui, C., Wang, D., Wang, H., Sun, J., Sun, W., Xiong, L.: Supercond. Sci. Technol. **33**, 03LT01 (2020)
4. Hahn, S., Kim, K., Kim, K., Hu, X., Painter, T., Dixon, I., Kim, S., Bhattarai, K.R., Noguchi, S., Jaroszynski, J., Larbalestier, D.C.: Nature **570**, 7762 (2019)
5. Chan, W.K., Schwartz, J.: Supercond. Sci. Technol. **30**, 074007 (2017)
6. Wang, Y., Chan, W.K., Schwartz, J.: Supercond. Sci. Technol. **29**, 045007 (2016)
7. Liu, D., Li, D., Zhang, W., Yong, H., Zhou, Y.: Supercond. Sci. Technol. **34**, 025014 (2021)
8. Wulff, A.C., Abrahamsen, A.B., Insinga, A.R.: Supercond. Sci. Technol. **34**, 053003 (2021)
9. Yan, Y., Song, P., Xin, C., Guan, M., Li, Y., Liu, H., Qu, T.: Supercond. Sci. Technol. **34**, 085012 (2021)
10. Yan, Y., Li, Y., Qu, T.: Supercond. Sci. Technol. **35**, 014003 (2021)
11. Maeda, H., Yanagisawa, Y.: IEEE Trans. Appl. Supercond. **24**, 4602412 (2014)
12. Xia, J., Bai, H., Yong, H., Weijers, H.W., Painter, T.A., Bird, M.D.: Supercond. Sci. Technol. **32**, 095005 (2019)
13. Yanagisawa, Y., Kominato, Y., Nakagome, H., Fukuda, T., Takematsu, T., Takao, T., Takahashi, M., Maeda, H., Conf, A.I.P.: Proc. **1434**, 1373–1380 (2012)
14. Amemiya, N., Akachi, K.: Supercond. Sci. Technol. **21**, 095001 (2008)
15. Koyama, Y., Takao, T., Yanagisawa, Y., Nakagome, H., Hamada, M., Kiyoshi, T., Takahashi, M., Maeda, H.: Physica C **469**, 694 (2009)
16. Barth, C., Komorowski, P., Vonlanthen, P., Herzog, R., Tediosi, R., Alessandrini, M., Bonura, M., Senatore, C.: Supercond. Sci. Technol. **32**, 075005 (2019)
17. Park, D., Bascunan, J., Li, Y., Lee, W., Choi, Y., Iwasa, Y.: IEEE Trans. Appl. Supercond. **31**, 4300206 (2021)
18. Hahn, S., Kim, Y., Ling, J., Voccio, J., Park, D.K., Bascunan, J., Shin, H.J., Lee, H., Iwasa, Y.: IEEE Trans. Appl. Supercond. **23**, 4601705 (2013)
19. Wang, Y., Weng, F., Li, J., Souc, J., Gomory, F., Zou, S., Zhang, M., Yuan, W.: IEEE Trans. Electrification. **6**, 1613 (2020)
20. Lécrevisse, T., Badel, A., Benkel, T., Chaud, X., Fazilleau, P., Tixador, P.: Supercond. Sci. Technol. **31**, 055008 (2018)
21. Painter, T., et al.: Design, construction and operation of a 13 T 52 mm no insulation REBCO insert for a 20 T all superconducting user magnet 25th International Conf. on Magnet Technology (Amsterdam), Or31–03 (2017). https://indico.cern.ch/event/445667/contributions/2562082/
22. Yanagisawa, K., Iguchi, S., Xu, Y., Li, J., Saito, A., Nakagome, H., Takao, T., Matsumoto, S., Hamada, M., Yanagisawa, Y.: IEEE Trans. Appl. Supercond. **26**, 4602304 (2016)
23. Bhattarai, K.R., Kim, K., Kim, K., Radcliff, K., Hu, X., Im, C., Painter, T., Dixon, I., Larbalestier, D., Lee, S., Hahn, S.: Supercond. Sci. Technol. **33**, 035002 (2020)
24. Benkel, T., Richel, N., Badel, A., Chaud, X., Lecrevisse, T., Borgnolutti, F., Fazilleau, P., Takahashi, K., Awaji, S., Tixador, P.: IEEE Trans. Appl. Supercond. **27**, 4602105 (2017)
25. Song, J.-B., Hahn, S., Lécrevisse, T., Voccio, J., Bascuñán, J., Iwasa, Y.: Supercond. Sci. Technol. **28**, 114001 (2015)
26. Markiewicz, W.D., Jaroszynski, J.J., Abraimov, D.V., Joyner, R.E., Khan, A.: Supercond. Sci. Technol. **29**, 025001 (2016)
27. Noguchi, S., Park, D., Choi, Y., Lee, J., Li, Y., Michael, P.C., Bascunan, J., Hahn, S., Iwasa, Y.: IEEE Trans. Appl. Supercond. **29**, 4301005 (2019)
28. Mato, T., Hahn, S., Noguchi, S.: IEEE Trans. Appl. Supercond. **31**, 4602405 (2021)
29. Noguchi, S.: IEEE Trans. Appl. Supercond. **29**, 4602607 (2019)
30. Markiewicz, W.D., Painter, T., Dixon, I., Bird, M.: Supercond. Sci. Technol. **32**, 105010 (2019)
31. Mataira, R.C., Ainslie, M.D., Badcock, R.A., Bumby, C.W.: Supercond. Sci. Technol. **33**, 08LT01 (2020)
32. Mataira, R., Ainslie, M.D., Badcock, R., Bumby, C.W.: IEEE Trans. Appl. Supercond. **31**, 4602205 (2021)
33. Duan, P., Ren, L., Li, X., Xu, Y., Li, J., Shi, J., Tang, Y., Guo, S.: IEEE Trans. Appl. Supercond. **31**, 4903305 (2021)
34. Hong, Z., Campbell, A.M., Coombs, T.A.: Supercond. Sci. Technol. **19**, 1246 (2006)

35. Wang, Y., Zhang, M., Yuan, W., Hong, Z., Jin, Z., Song, H.: J. Appl. Phys. **122**, 053922 (2017)
36. Rhyner, J.: Physica C **212**, 292 (1993)
37. Grilli, F., Sirois, F., Zermeno, V.M., Vojenčiak, M.: IEEE Trans. Appl. Supercond. **24**, 8000508 (2014)
38. Zhong, Z., Wu, W., Jin, Z.: Supercond. Sci. Technol. **34**, 08LT01 (2021)
39. Zhong, Z., Wu, W., Wang, L., Li, X.-F., Li, Z., Hong, Z., Jin, Z.: J. Supercond. Nov. Magn. **34**, 2809 (2021)
40. Wang, X., Sheng, J., Zhong, Z., Wu, W., Li, X.-F., Jin, Z., Hong, Z.: Supercond. Sci. Technol. **34**, 065007 (2021)
41. Lu, J., Levitan, J., McRae, D., Walsh, R.: Supercond. Sci. Technol. **31**, 085006 (2018)
42. Michael, P.C., Park, D., Choi, Y.H., Lee, J., Li, Y., Bascunan, J., Noguchi, S., Hahn, S., Iwasa, Y.: IEEE Trans. Appl. Supercond. **29**, 4300706 (2019)
43. Zhong, Z., Wu, W., Wang, X., Li, X.-F., Sheng, J., Hong, Z., Jin, Z.: Supercond. Sci. Technol. **34**, 025016 (2021)
44. Jin, J., Zhou, Q., Wu, W., Mei, E., Sun, L., Zhang, G., Du, J., Liu, T., Jiang, S., Qin, J., Zhou, C., Jin, H., Jin, Z., Sheng, J., Li, Z., Wang, S., Gu, B., Liu, L., Yang, X., Zhao, Y.: IEEE Trans. Appl. Supercond. **31**, 4002817 (2021)
45. Rossi, L., Badel, A., Bajko, M., Ballarino, A., Bottura, L., Dhalle, M.M.J., Durante, M., Ph Fazilleau, J., Fleiter, W., Goldacker, E., Haro, A., Kario, G., Kirby, C., van Lorin, J., de Nugteren, G., Rijk, T., Salmi, C., Senatore, A., Stenvall, P., Tixador, A., Usoskin, G., Volpini, Y.Y., Zangenberg, N.: IEEE Trans. Appl. Supercond. **25**, 4001007 (2015)
46. Anderson, P.W.: Phys. Rev. Lett. **9**, 309 (1962)
47. Bean, C.P.: Rev. Mod. Phys. **36**(1), 31 (1964)
48. Hu, X., Small, M., Kim, K., Kim, K., Bhattarai, K., Polyanskii, A., Radcliff, K., Jaroszynski, J., Bong, U., Park, J.H., Hahn, S., Larbalestier, D.: Supercond. Sci. Technol. **33**, 095012 (2020)
49. Mori, S., Noguchi, S.: IEEE Trans. Appl. Supercond. **31**, 8400305 (2021)